



# Mechanics of tissue rupture during needle insertion in transverse isotropic soft tissue

Wanyu Liu<sup>1</sup> · Zhiyong Yang<sup>1</sup> · Pan Li<sup>1</sup> · Jianpeng Zhang<sup>1</sup> · Shan Jiang<sup>1</sup>

Received: 17 May 2018 / Accepted: 24 January 2019 / Published online: 21 February 2019  
© International Federation for Medical and Biological Engineering 2019

## Abstract

During robot-assisted percutaneous puncture surgery, a bevel-tipped needle is inserted into a fiber-structured soft tissue, which has transverse isotropic mechanical properties. Tissue rupture may lead to needle bending and insertion error. Therefore, analysis of the mechanics of rupture events in transverse isotropic space is essential for the precise control of needle motion. We analyzed the needle stiffness force and the cutting force, both related to rupture events, which are caused by contact deformation and tissue cutting, respectively. A modified model based on a homogeneous elastic half-space contact force model was used to describe the variation in the stiffness force of the needle. An energy-based maximum stiffness force model was proposed to predict the surface rupture for a needle that is inserted at different orientations. A model for the cutting force was presented based on a solid mechanics theory of unidirectional fiber-reinforced composite material to analyze the effect of the needle tip pose on the cutting force. Experiments on porcine muscle confirmed that the stiffness force and the cutting force were clearly influenced by the insertion orientation angle. The developed models could predict the stiffness force and the cutting force during needle insertion into the transverse isotropic tissue. This method provides a foundation for predicting needle deflection in the transverse isotropic space.

**Keywords** Fiber-structured soft tissue · Cutting force · Stiffness force · Insertion orientation · Needle tip pose

## 1 Introduction

Robotics-assisted technology for automatic needle insertion is an important research topic in surgical procedures that involve percutaneous puncture. One of the fundamental problems of this type of technology is to model the interaction force of the needle and the soft tissue [11–13, 20]. The interaction force would cause soft tissue deformation and needle deflection, which are two important causes of insertion error [3, 7].

The needle is a research tool for analyzing the interaction force (also called the “insertion force”). The insertion force can be used to predict needle deflection and to provide a way to monitor the safety of a surgical procedure that involves percutaneous puncture [1, 15, 23].

Numerous researchers have developed models of the needle insertion force by assuming that the soft tissue is an

isotropic linear elastic/viscoelastic solid [1–3, 11, 25]. During needle insertion into the soft tissue, three phases are evident [13, 16, 17, 20]. The first phase is the “external contact deformation,” in which the needle tip makes contact with the tissue surface. The contact force acting on the needle tip (called the “stiffness force”) is ever-increasing before the tissue surface is punctured. The second phase relates to the surface that has been punctured. When tissue deformation reaches a limit, the stiffness force also reaches its maximum value, and the tissue surface cracks suddenly and propagates into the tissue. The third phase is the “internal insertion movement.” The surface crack propagates into the tissue in response to needle displacement, and the tissue is cut by the needle tip. The cutting force acts on the bevel of the needle tip. Friction is applied tangentially to the needle shaft and resists the motion of the needle.

Before the third phase, the insertion force equals the stiffness force. Then, in the third phase, the insertion force is the summation of the cutting force and the friction force. Okamura et al. [20] measured the insertion force and simulated it using a “nonlinear spring model” for the stiffness force, a modified Karnopp’s model for the friction, and a constant

✉ Shan Jiang  
shanjmri@tju.edu.cn

<sup>1</sup> School of Mechanical Engineering, Tianjin University, No. 135, Yaguan Road, Jinnan District, Tianjin City 300354, China

value for the cutting force. Jiang et al. [11] described the contact stage as an axisymmetric Boussinesq problem. The cutting force was expressed as a constant value by considering the same work done by Hing [10].

Other works regarding more detailed questions, such as the effect of tissue viscoelasticity and rupture events on the insertion force, have also been studied. Barnett [3] concluded that 61% of the total insertion force arises from creating the crack. The J-integral method from the fracture mechanics has been used to analyze the rupture events in tissue, and fracture toughness is an important mechanical parameter for estimating the fracture generation [3, 13, 16, 17]. Mahvash [17] employed a modified nonlinear viscoelastic Kelvin model, and Khadem [13] adopted a standard linear solid to predict the force-deformation response of a needle that comes in contact with a tissue. Tanaka [27] was the first to propose a single-layer three-dimensional (3D) tissue model (i.e., a direction-dependent response and coupling effect) to describe the inherent viscoelastic characteristics of the human skin.

In further application studies, Khadem [12] showed a method for predicting needle deflection for a cutting force that acts on a needle tip. Abayazid [1] proposed a mechanics-based model in his doctoral dissertation to predict needle deflection. The purpose of these works was to steer needle insertion accurately.

All of the works mentioned previously considered the tissue to be a type of isotropic solid. However, during percutaneous puncture, the needle must insert through the skin and the muscle, which have a fiber structure and inhomogeneous mechanical properties [6, 21, 30].

Using tensile rupture testing, Wong [30] provided evidence that the tissue modulus of elasticity and fracture-related properties are sensitive to varying fiber orientations. The studies of Ottenio [21] and Ni Annaidh [18, 19] suggested that the direction of the arrangement of collagen fibers has a significant influence on the mechanics of the human skin. Hence, skin should be described as a “transverse isotropic material” [4, 22, 24].

Furthermore, numerous researchers have attempted to characterize the mechanical properties of muscle with different fiber orientations [5, 9, 28, 29]. Typically, Böll [6] provided experimental evidence that the direction of the muscle fibers contributes to compressive stress. The tensile experiments in studies by Takaza [26] showed that the muscle fiber direction has an obvious effect on tissue failure.

In summary, fiber structure means that the tissue has transverse isotropic mechanical properties that are closely related to rupture events. To improve the model’s predicted accuracy of the stiffness force and the cutting force, we analyzed the mechanics of needle tip interaction with transverse isotropic tissue during needle insertion by assuming that the soft tissue is a unidirectional fiber-reinforced composite material.

## 2 Methods

### 2.1 Model development

In this section, mechanics-based models were developed to estimate the stiffness force and the cutting force of the needle. We separated the needle insertion process into the following two stages: external contact and inside cutting.

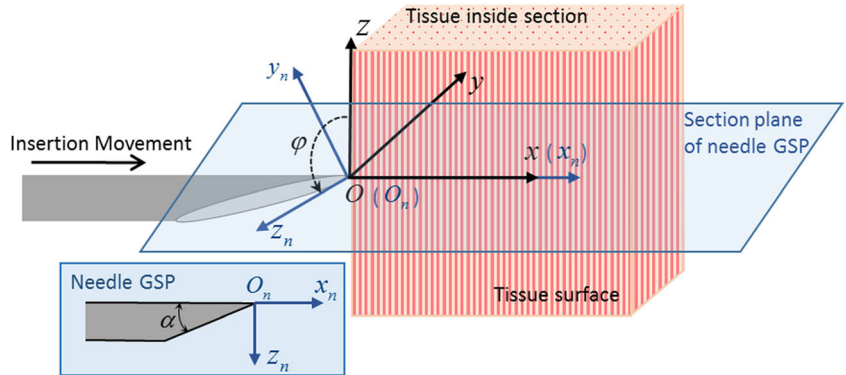
First, we established the orientation relationship of the needle and the transverse isotropic tissue. In Fig. 1, two Cartesian coordinate systems are fixed, which are as follows: one is at the contact point on the tissue surface and is marked  $O\text{-}xyz$  and the other is on the needle tip and is marked  $O_n\text{-}x_n\text{-}y_n\text{-}z_n$ . In normal conditions, the surface of the transverse isotropic soft tissue is in the orthogonal plane. Thus, we placed the  $z$ -axis on the fiber line. Furthermore, the direction of the  $x$ -axis is the same as that of the insertion movement. Then, the  $x\text{-}O\text{-}y$  plane represents the isotropic plane of the tissue. Therefore,  $O\text{-}xyz$  represents the principal elasticity directions of the tissue material. The orientation of  $x_n$  is consistent with the  $x$ -axis, and the geometric symmetry plane (GSP) of the needle is in the plane  $x_n\text{-}O_n\text{-}z_n$ , which includes a positive direction of the  $z_n$ -axis point to the short side of the needle GSP (Fig. 1). Hence, the orientation of the coordinate system  $O_n$  was confirmed. The relationship between the two coordinate systems was also perceived:  $O_n$  “rolled” around the  $x_n$ -axis counterclockwise from the orientation registration with  $O$  until plane  $x_n\text{-}O_n\text{-}z_n$  contained the GSP of the needle. We named the rotation angle as the “insertion orientation angle” (IOA) of the needle and marked it as  $\varphi$ .

#### 2.1.1 Force model of external contact

To clearly explain the mechanics of the external contact phase, we divided the stiffness force into two stages. The first stage was tissue deformation (i.e., the needle tip makes contact with the tissue surface at a point, and, then, the tissue is deformed by the pushing of the needle). The stiffness force keeps increasing in this stage. The second stage was surface rupture. Here, the stiffness force and the tissue deformation reach their maximum values, and the tissue surface is ruptured at that moment. We can explain the mechanical events in reverse order.

Under the insertion force of the needle, the tissue surface is cut by the bevel of the needle tip, and, at that moment, there is a crack initiation along the direction of the opening angle of the needle tip. According to the definition of local failure, once the energy that is released through a crack extension equals to or exceeds the unit area fracture toughness  $G_c$  ( $\text{kN}/\text{m}^3$ ), the material initiates cracking. The different directions of the opening angle of the needle tip in relation to the direction of the fiber result in different maximum values of the stiffness force at the moment of fracture of the tissue surface.

**Fig. 1** A coordinate diagram of needle insertion into the transverse isotropic soft tissue with a random IOA of the needle



Two parameters of fracture mechanics, including the crack tip opening displacement (CTOD)  $\delta$  and the  $J$  contour integral, are used widely to characterize crack initiation and crack growth within materials. Here, we modified the model of Khadem et al. [13], which employed a strip yield model to calculate the CTOD and the  $J$  contour integral to describe crack initiation under the coordinate system  $O_n$  in the transverse isotropic tissue.

The  $J$  integral is used to measure the energy release rate per unit of crack advance in the soft tissue. Figure 2a shows a strip yield zone around the needle tip with length  $\rho$  and corresponding  $\delta$  at the moment the tissue surface is ruptured.  $\Gamma$  is an arbitrary curve that starts under the surface and runs counter-clockwise around the crack tip to its upper surface. The  $J$  integral is given by:

$$J = \int_{\Gamma} \left( W dz_n - \mathbf{T}_g \frac{\partial \mathbf{u}}{\partial x_n} ds \right) = \int_{\Gamma} \left( W dz_n - T_i \frac{\partial u_i}{\partial x_n} ds \right) \quad (1)$$

$$T_i = \sigma_{ik} n_k \quad (2)$$

where  $W$  is the strain energy;  $\sigma_{ik}$  are components of the stress tensor;  $T_i$  are force components that act on the unit length of  $\Gamma$ ;  $ds$  is the increment in arc length along  $\Gamma$ ;  $n_k$  are components of the outer normal unit vector; and  $u_i$  are displacement vector components on  $\Gamma$ . Considering that the

direction of  $\delta$  almost coincides with the direction of the  $z_n$ -axis and the value of  $\delta$  is relatively small (its maximum value during insertion approximate to the needle outer diameter, i.e.  $\delta \approx d \approx 1.5\text{mm}$ ), the first term in the integral in Eq. (1) vanishes because  $dz_n = 0$ . In addition, considering that only surface tension is present in the direction of the  $z_n$ -axis, there are no force components in the directions of the  $x_n$ -axis and the  $y_n$ -axis; i.e.,  $n_{x_n} = n_{y_n} = 0$  and  $n_{z_n} = 1$ . Hence, Eq. (1) can be simplified to:

$$J = \int_{\Gamma} \sigma_{z_n z_n} \frac{\partial u_{z_n}}{\partial x_n} ds \quad (3)$$

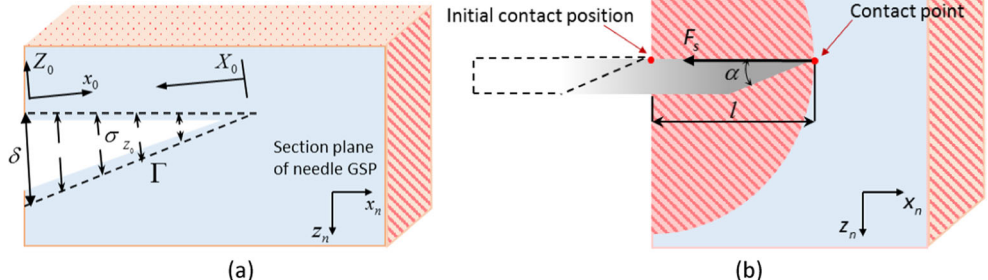
Then, a new coordinate  $X_0 Z_0$  is defined at the crack tip with  $X_0 = \rho - x_0$ . Hence,  $\sigma_{z_n z_n}$  and  $u_{z_n}$  are related only to  $X_0$  and  $u_{z_n}(X_0 = \rho) = \delta/2$ ; so, Eq. (3) can be written as:

$$J = 2 \int_0^{\rho} \sigma_{z_n z_n}(X_0) \frac{\partial u_{z_n}(X_0)}{\partial X_0} dX_0 = \int_0^{\delta} \sigma_{z_n z_n}(\delta) d\delta \quad (4)$$

At the moment the tissue surface is ruptured,  $\sigma_{z_n z_n} = \sigma_{Z_0}$ , and  $\sigma_{Z_0}$  is the maximum yield stress acting on the crack surface. Thus, we have:

$$J = \sigma_{Z_0} \delta \quad (5)$$

**Fig. 2** Force model of external contact (schematic). **a** The strip yield zone around the needle tip and corresponding CTOD at the moment the tissue surface is ruptured. **b** External contact deformation of the transverse isotropic soft tissue



Now, we can focus on the rupture on a transverse isotropic material. The rupture happens perpendicular to the fibers when  $\varphi = 0$ , whereas it happens primarily parallel to the fibers when  $\varphi = \pm \pi/2$ . Considering the elastic symmetry of the transverse isotropic material, we employed fracture toughness  $G_c$  as a function with an independent variable denoted by  $\phi$  (where  $\phi = |\sin \varphi|$ ). Now, we can estimate the power  $U$  of the needle tip that is needed at the moment of insertion into the tissue surface:

$$U = G_c(\phi)a\delta \quad (6)$$

where  $a$  is the total length of the needle tip that is inserted into the tissue surface at the moment of rupture, and it can be represented approximately as:

$$a = d/(2\tan(\alpha/2)) \quad (7)$$

Here, we define  $d$  as the outer diameter of the needle and  $\alpha$  as the sharp angle of the needle tip. At the moment of rupture, the maximum stiffness force along the needle axis can be written as:

$$F_{smax} = 2\sigma_{z0}aA\sin(\alpha/2) \quad (8)$$

where  $A$  is the contact area between the needle tip and the tissue. According to local failure criteria, we deemed  $U=J$  at that time. Therefore, by combining Eq. (5) and Eq. (8), we obtain:

$$F_{smax}(\phi) = \frac{G_c(\phi)dA\sin(\alpha/2)}{\tan(\alpha/2)} \quad (9)$$

Here, the maximum stiffness force  $F_{smax}$  during needle insertion into the transverse isotropic soft tissue with different IOAs is given by Eq. (9).

Now, we can discuss the mechanics at the stage of contact deformation. At this stage, the needle applies a vertical force on the orthogonal anisotropic surface of the soft tissue, and the needle axis is parallel to the isotropic plane of the tissue. Then, we extend the force deformation response model to the transverse isotropic half space by modifying the stiffness force model that was proposed by Jiang et al. [11]. The previous model described the stiffness force in the following form:

$$F_s = \frac{2}{\pi}El^2\tan(\alpha) \quad (10)$$

where  $l$  is the displacement of the needle tip along the insertion direction from the initial contact position and  $E$  represents the reduced modulus containing the elastic parameters of the needle and tissue. Now, for needle contact with the transverse isotropic soft tissue, we can display the deformation mechanism in Fig. 2b.

To characterize the coupling elastic of tissue, we introduce a reference elastic parameter  $C$  that can be determined by using the following equation:

$$C = 1 - v_T^2/E_T \quad (11)$$

where  $E_T$  and  $v_T$  are the equivalent elastic modulus and the equivalent Poisson ratio of the soft tissue, respectively. Both of these terms reflect the elastic coupling effect of the tissue in the contact stage. Then, we can determine the reduced modulus in a contact event with complex coupling elasticity:

$$E = \frac{E_n}{1 - v_n^2 + CE_n} \quad (12)$$

where  $E_n$  and  $v_n$  represent the Yang's modulus and the Poisson ratio of the needle, respectively. If the insertion speed is a time-dependent function  $V(t)$ , the displacement  $l(t)$  can be expressed as:

$$l(t) = \int_0^t V(t)dt \quad (13)$$

Thus, Eq. (10) can be rewritten as:

$$F_s(t) = \frac{2}{\pi}E\tan(\alpha)\left(\int_0^t V(t)dt\right)^2 \quad (14)$$

Using the model for the maximum stiffness force described in Eq. (9), at the moment of rupture, Eq. (9) will equal Eq. (14); whereupon, we obtain:

$$C = \frac{2\tan(\alpha)l^2}{\pi G_c(\phi)dA\cos(\alpha/2)} + \frac{v_n^2 - 1}{E_n} \quad (15)$$

$C$  is a variable that changes with  $\phi$ . Therefore, if the expression of  $G_c(\phi)$  is known, the stiffness force from the initial contact to the surface rupture could be predicted based on Eq. (9) and Eq. (14). To verify this method of stiffness force calculation, the expression of  $G_c(\phi)$  will be identified from the insertion experiments in Section 3.

### 2.1.2 Force model of cutting inner tissue

The phenomenon of a needle tip cutting tissue begins after the rupture of the tissue surface. At that time, the needle tip has inserted completely into the soft tissue. Throughout the insertion, the bevel plane of the needle tip continues to press the tissue it is in contact with, which produces a counterforce from the pressed tissue acting on the bevel plane of the needle tip so that the surface crack keeps extending into the tissue. The interaction force perpendicular to the contacting bevel plane is named the “cutting force.” Barnett [3] showed that the cutting force was almost independent of the insertion speed but was affected largely by the geometric features of the needle. Next, we developed a model of the cutting force in the

transverse isotropic space of the tissue without considering the insertion speed.

Tissue cutting is an instantaneous process, in which the initial crack on one point within the tissue grows to its maximum (approximately the outer diameter of the needle), and it only occurs around the needle tip. Compared with the insertion movement, extension of the initial crack has a relatively high speed, and the tissue deformation around the needle tip is small. Hence, in accordance with Khadem et al. [13], we considered the tissue near the needle tip to be a linear elastic material. By describing the cutting force as a distributed force along the plane of the needle tip bevel, the cutting phenomenon is shown in Fig. 3a, in which the needle tip is simplified to a wedge. The tip cutting event can be discretized into small incremental crack growths that are equal to the size of the needle tip. As shown in Fig. 3b, a series of “virtual springs” are fixed at a remote distance in the tissue, which will be compressed by the corresponding length of local “CTOD” in a direction that is perpendicular to the plane of the needle tip bevel. The compressions of these springs also increase with crack growth. The compressed springs are usually in the nonprincipal elasticity directions of the tissue; so, we can calculate the cutting force as:

$$F_c = \int_0^a E' \delta dX_0 \quad (16)$$

where  $a$  is the length of the needle tip and  $E'$  is the off-axis reduction stiffness coefficient of the tissue along the direction of the cutting force. It can also represent the stiffness of these virtual springs. From Fig. 3b, we can see that the  $\delta$  is variable with respect to the location of the virtual spring, which was fixed on the bevel of the needle tip. Hence, the value of the corresponding  $\delta$  can be calculated as follows:

$$\delta = 2X_0 \tan(\alpha/2) \quad (17)$$

Eq. (17) can be rewritten as:

$$F_c = E' a^2 \tan(\alpha/2) \quad (18)$$

The value of  $E'$  is anisotropic according to the different dimensional orientations of the needle tip in the tissue. Acquiring arbitrary  $E'$  from experiments directly is difficult.

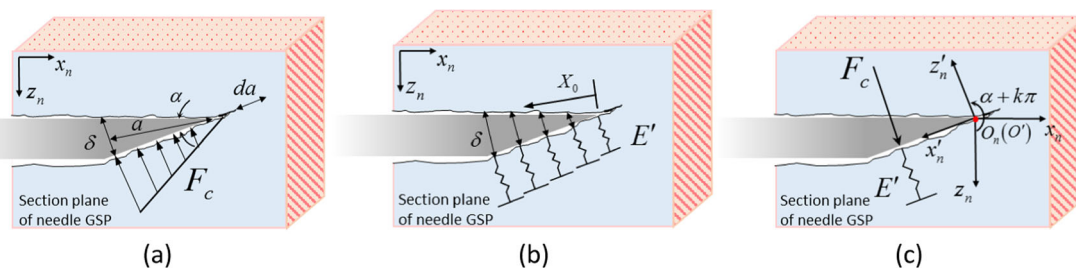


**Fig. 3** Cutting phenomenon of a needle moving in the transverse soft tissue. **a** Discretization of the cutting force along the plane of the needle tip bevel. **b** Model with “virtual springs” for the counterforce from the pressed soft tissue. **c** Coordinate transform diagram of  $E'$  in the transverse isotropic space

Therefore, we referred to the solid mechanics theory of unidirectional fiber-reinforced composite materials [8] to deduce the expression of an off-axis reduction stiffness coefficient during insertion into transverse isotropic tissue with an arbitrary IOA.

The stiffness matrix of the principal direction of the tissue is a compliance matrix of a transversely isotropic material and is given by:

$$\hat{\mathbf{C}} = \begin{bmatrix} \hat{C}_{11} & \hat{C}_{12} & \hat{C}_{13} & 0 & 0 & 0 \\ \hat{C}_{21} & \hat{C}_{22} & \hat{C}_{23} & 0 & 0 & 0 \\ \hat{C}_{31} & \hat{C}_{32} & \hat{C}_{33} & 0 & 0 & 0 \\ 0 & 0 & 0 & \hat{C}_{44} & 0 & 0 \\ 0 & 0 & 0 & 0 & \hat{C}_{55} & 0 \\ 0 & 0 & 0 & 0 & 0 & \hat{C}_{66} \end{bmatrix} \quad (19)$$

where

$$\left. \begin{array}{l} \hat{C}_{11} = \hat{C}_{22} \\ \hat{C}_{12} = \hat{C}_{21} \\ \hat{C}_{13} = \hat{C}_{31} = \hat{C}_{23} = \hat{C}_{32} \\ \hat{C}_{44} = \hat{C}_{55} \\ \hat{C}_{66} = (\hat{C}_{11} - \hat{C}_{12})/2 \end{array} \right\} \quad (20)$$

Subscripts 1, 2, and 3 represent the x-axis, y-axis, and z-axis of the tissue principal direction, respectively. Hence, there are 5 independent elastic constants in the stiffness matrix of the tissue:  $\hat{C}_{11}$ ,  $\hat{C}_{12}$ ,  $\hat{C}_{13}$ ,  $\hat{C}_{33}$ , and  $\hat{C}_{44}$ .

Now, we can introduce the principle of tensor transformation to transform the elastic characteristics of the tissue to describe it in the needle-related system. First, the transformation relationship from the Cartesian coordinate systems  $O$  to  $O_n$  is given in Table 1.

Then, we only need to consider the  $x_n o_n z_n$  plane, which contains the GSP of the needle. The stiffness matrix in the plane is defined as:

$$\hat{\mathbf{C}}^n = \begin{bmatrix} \hat{C}_{11}^n & \hat{C}_{13}^n & \hat{C}_{15}^n \\ \hat{C}_{31}^n & \hat{C}_{33}^n & \hat{C}_{35}^n \\ \hat{C}_{51}^n & \hat{C}_{53}^n & \hat{C}_{55}^n \end{bmatrix} \quad (21)$$

**Table 1** Transform parameters from system  $O$  to system  $O_n$ 

$\hat{l}_{ij}$	$x$	$y$	$z$
$x_n$	1	0	0
$y_n$	0	$\cos\varphi$	$\sin\varphi$
$z_n$	0	$-\sin\varphi$	$\cos\varphi$

$$\hat{C}_{ij}^n = \sum \hat{C}_{mn} \hat{l}_{im}^c \hat{l}_{jn}^c \quad (22)$$

The corresponding relationship among the transform parameters  $\hat{l}_{im}^c$ ,  $\hat{l}_{jn}^c$ , and  $\hat{l}_{ij}$  is shown in Table 2.

Through the tensor transformation, we obtain:

$$\left. \begin{aligned} \hat{C}_{11}^n &= \hat{C}_{11} \\ \hat{C}_{13}^n &= \hat{C}_{31}^n = \hat{C}_{12} \\ \hat{C}_{33}^n &= \hat{C}_{11}(S^4 + 2C^2S^2) + 2C^2S^2(\hat{C}_{13} - \hat{C}_{12}) + \hat{C}_{33}C^4 \\ \hat{C}_{55}^n &= \hat{C}_{44}C^2 + \frac{\hat{C}_{11} - \hat{C}_{12}}{2}S^2 \\ \hat{C}_{15}^n &= \hat{C}_{51}^n = \hat{C}_{35}^n = \hat{C}_{53}^n = 0 \end{aligned} \right\} \quad (23)$$

where  $C$  is  $\cos\varphi$  and  $S$  is  $\sin\varphi$ . Next, we contra-rotate the  $O_n$  around the  $y_n$  axis with  $\alpha + k\pi$  ( $k$  is an integer), as shown in Fig. 3c. In this way, we obtain an off-axis coordinate system  $O'_n - x'_n y'_n z'_n$ , which equips the  $z'_n$ -axis that represents the direction of the virtual springs. Finally, using the tensor transformation again, we confirmed the expression of  $E'$  as:

$$E' = s^4 \hat{C}_{11}^n + c^4 \hat{C}_{33}^n + 2c^2s^2 \hat{C}_{13}^n + 4c^2s^2 \hat{C}_{55}^n \quad (24)$$

where  $c$  is  $\cos(\alpha + k\pi)$  and  $s$  is  $\sin(\alpha + k\pi)$ . Combining Eq. (23) and Eq. (24), we deduce two forms of expression of an off-axis reduction stiffness coefficient.

$$\begin{aligned} E' &= \hat{C}_{11}(s^4 + c^4S^4 + 2c^4C^2S^2 + 2c^2s^2S^2) \\ &+ \hat{C}_{33}c^4C^4 + \hat{C}_{12}(2c^2s^2 - 2c^2s^2S^2 - 2c^4C^2S^2) \\ &+ 2\hat{C}_{13}c^4C^2S^2 + 4\hat{C}_{44}s^2C^2 \end{aligned} \quad (25a)$$

$$\begin{aligned} E' &= \phi^4 c^4 (\hat{C}_{33} - \hat{C}_{11} - 2\hat{C}_{13} + 2\hat{C}_{12}) + \\ &2\phi^2 [c^2s^2 (\hat{C}_{11} - \hat{C}_{12} - 2\hat{C}_{44}) + c^4 (\hat{C}_{11} + \hat{C}_{13} - \hat{C}_{33} - \hat{C}_{12})] + \\ &c^4 \hat{C}_{33} + 4c^2s^2 \hat{C}_{44} + s^4 \hat{C}_{11} + 2c^2s^2 \hat{C}_{12} \end{aligned} \quad (25b)$$

The values of the 5 independent elastic constants of the tissue could be obtained from experiments. By substituting them into Eq. (25b) and combining with Eq. (18), the cutting force can be predicted when the needle tip moves inside of the transverse isotropic soft tissue with any IOA.

## 2.2 Experimental procedures

### 2.2.1 Experimental setup

The two degrees of freedom (DOF) mechanical setup shown in Fig. 4a was used to carry out experiments on automatic needle insertion. For movement of needle insertion and IOA adjustment, the setup was equipped with two respective drive structures. One was a linear motor (MSMJ012G1 V; Panasonic, Tokyo, Japan) that is controlled by the same-brand motion controller (MADKT1505CA1) and actuated a lead-screw mechanism. The other was a step servo rotary motor (AM11SS1DMA; MOONS, Shanghai, China) that is controlled by the same-brand motion controller (SS03-S-A). A standard 17-G stainless steel brachytherapy needle of 1.47 mm diameter and 30° beveled tip (Mick Radio-Nuclear Instruments, New York, USA) was used for insertion into the porcine muscle. A 6-DOF force/torque (F/T) sensor (Nano17; ATI Industrial Automation, Apex, NC, USA) was installed at the needle base to obtain data on the insertion force. The z-axis of the force sensor coincided with the needle axis.

Two fresh single muscles were obtained from the same site of two porcine tenderloins that were purchased from a local slaughterhouse. One of the muscle samples was dissected along the orientation of the surface fibers (Fig. 4b). The fiber orientation within the muscle sample was consistent with those that were visible on the surface. Therefore, we could

**Table 2** Relationship among transform parameters

$\hat{l}_{ij}^c$	1	2	3	4	5	6
1	$\hat{l}_{11}^2$	$\hat{l}_{12}^2$	$\hat{l}_{13}^2$	$2\hat{l}_{12}\hat{l}_{13}$	$2\hat{l}_{13}\hat{l}_{11}$	$2\hat{l}_{12}\hat{l}_{11}$
2	$\hat{l}_{21}^2$	$\hat{l}_{22}^2$	$\hat{l}_{23}^2$	$2\hat{l}_{23}\hat{l}_{22}$	$2\hat{l}_{23}\hat{l}_{21}$	$2\hat{l}_{22}\hat{l}_{21}$
3	$\hat{l}_{31}^2$	$\hat{l}_{32}^2$	$\hat{l}_{33}^2$	$2\hat{l}_{33}\hat{l}_{32}$	$2\hat{l}_{33}\hat{l}_{31}$	$2\hat{l}_{32}\hat{l}_{31}$
4	$\hat{l}_{31}\hat{l}_{21}$	$\hat{l}_{32}\hat{l}_{22}$	$\hat{l}_{33}\hat{l}_{23}$	$\hat{l}_{33}\hat{l}_{22} + \hat{l}_{32}\hat{l}_{23}$	$\hat{l}_{33}\hat{l}_{21} + \hat{l}_{31}\hat{l}_{23}$	$\hat{l}_{31}\hat{l}_{22} + \hat{l}_{32}\hat{l}_{21}$
5	$\hat{l}_{31}\hat{l}_{11}$	$\hat{l}_{32}\hat{l}_{12}$	$\hat{l}_{33}\hat{l}_{13}$	$\hat{l}_{33}\hat{l}_{12} + \hat{l}_{32}\hat{l}_{13}$	$\hat{l}_{33}\hat{l}_{11} + \hat{l}_{31}\hat{l}_{13}$	$\hat{l}_{31}\hat{l}_{12} + \hat{l}_{32}\hat{l}_{11}$
6	$\hat{l}_{21}\hat{l}_{11}$	$\hat{l}_{12}\hat{l}_{22}$	$\hat{l}_{13}\hat{l}_{23}$	$\hat{l}_{13}\hat{l}_{22} + \hat{l}_{12}\hat{l}_{23}$	$\hat{l}_{13}\hat{l}_{21} + \hat{l}_{11}\hat{l}_{23}$	$\hat{l}_{11}\hat{l}_{22} + \hat{l}_{12}\hat{l}_{21}$

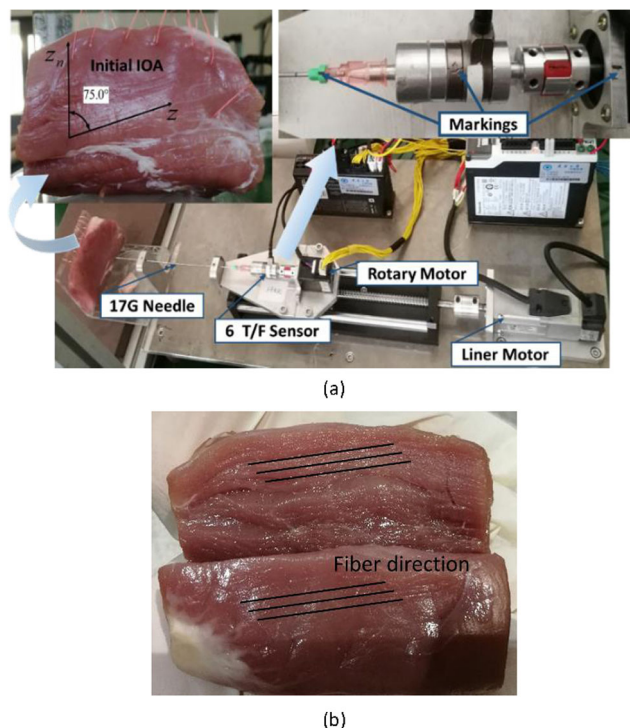


**Fig. 4** Experimental setup for automatic needle insertion. **a** Initial identification of the IOA before the insertion experiments. **b** Fiber orientation of the muscle sample

confirm the fiber orientation of a single muscle sample by direct visualization.

As shown in Fig. 4a, we marked lines to represent the needle GSP, the y-axis of the sensor, and the axis direction of the rotary motor. Then, we adjusted the marked lines to lie in the same plane to make the GSP of the needle perpendicular to the horizontal plane. Then, another muscle sample was fixed on a support that is perpendicular to the horizontal plane. To predefine the relative angle between the needle and tissue fibers, we took a photograph of the fixed sample using a calibrated horizontal high-speed camera before testing. From the photograph, we could measure the angle between the fiber orientation and the perpendicular, which was  $75^\circ$  (Fig. 4a). Hence, the initial insertion orientation angle was  $75^\circ$  in our experiments.

A full test process had the following three steps: (a) insertion (needle was inserted into the muscle sample); (b) no motion (needle stops and is held within the sample); (c) extraction (needle is extracted from the sample). To minimize the effect of needle bending on force data, the length of the needle inserted in all experiments was  $\approx 40$  mm. The speed of the needle movement was 1 mm/s and was controlled by the linear motor. The 6-DOF (F/T) sensor collected data on the force and torque acting on the needle base during the test. The needle did not rotate during needle–tissue interaction; so, we needed to analyze only the force data.

## 2.2.2 Experimental scenarios and the data-processing method

Before experimentation, we conducted a pretest of the needle insertion with an initial IOA and collected the force data in three directions during this process. The sensor-measured force is shown in Fig. 5.  $F_x$  and  $F_y$  were caused by needle bending and some part of the cutting force.  $F_z$  is the needle axial insertion force. The increases in  $F_x$  and  $F_y$  were very small, and their values were close to zero. Hence, for a needle insertion length of  $\approx 40$  mm, we could neglect the effect of needle bending on the insertion force.

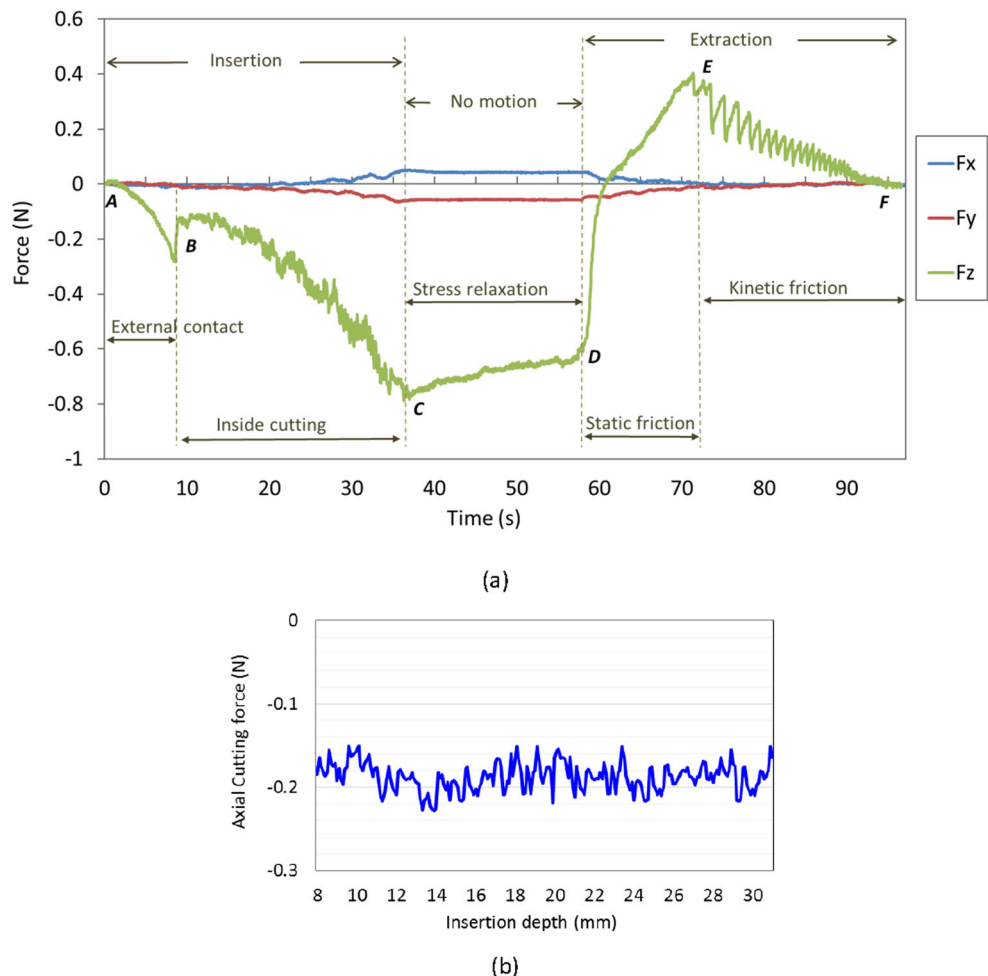
In Fig. 5a, we could divide the data on the insertion force into the following five parts:

- From A to B: The needle began to make contact with surface of the muscle sample at the time of point A. Then, the tissue continued to be deformed until the time of point B, at which point the surface ruptured and the stiffness force reached a maximum value.
- From B to C: This was the inside cutting stage. The insertion force was the result of the cutting force and friction.
- From C to D: The feeding mechanism stopped and remained static for a few seconds to avoid the influence of an inertial force in the extraction stage. The force data during this stage were nonzero. This effect was probably due to the characteristics of stress relaxation and the deformation of the soft tissue [14].
- From D to E: The needle was extracted from the sample at the time of point D. From D to E, because of the “spring back” and viscous effect of tissue, there was no relative motion between the needle and the sample, and a static friction force acted on their contact area.
- From E to F: The needle began gradually moving relative to the sample. There was only friction in this stage until the needle was withdrawn from the sample.

By inverted-sequence subtraction of the friction of part (e) from part (b), we could obtain data on the cutting force that was measured along the direction of the needle axis. To eliminate or minimize the influence of an unsteady cutting motion of the needle, we chose the middle part of the cutting force data to describe stable tissue cutting. As shown in Fig. 5b, an axial cutting force fluctuated within a certain narrow range that could be considered to be a constant. Hence, we took the mean value of the data to represent the axial cutting force for the corresponding IOA.

Then, a series of needle insertion experiments were carried out on porcine muscle. We determined the mechanical parameters of the tissue by using the inverse model. In the experiments, we performed ten groups of integrated tests using the same process as that employed in the pretest. Before each group of integrated tests, the IOA of the needle was increased

**Fig. 5** Processing of data on insertion force. **a** Analyses from a sensor-measuring force in the pretest. **b** Data on the axial cutting force of a stable cutting motion during the inside cutting stage in the pretest



15° clockwise by controlling the rotary motor. Hence, a series of values of IOA from 75° to 210° was applied separately in ten groups of the integrated tests. Each group of the integrated tests contained 10 trials of the full process of movement of needle insertion and needle extraction. A similar method of data analysis to that used in the pretest was used in the experiments.

### 3 Results

Based on the experimental data, the first nine trials' maximum stiffness force of each group was used in Eq. (9) to calculate the corresponding fracture toughness  $G_c$ . Then, we fit these values of  $G_c$  to identify the expression of  $G_c(\phi)$  using the method of least squares. With a goodness-of-fit  $R^2 = 0.9973$ , we obtained the expression of  $G_c(\phi)$  in Eq. (27).

$$G_c(\phi) = 0.5619\phi^3 - 0.7427\phi^2 + 0.2994\phi - 0.1616 \quad (27)$$

To obtain the reference elastic parameter  $C$ , the first nine trials of the experimental force data in part (a) of each group of the test were used for fitting the model of stiffness force given

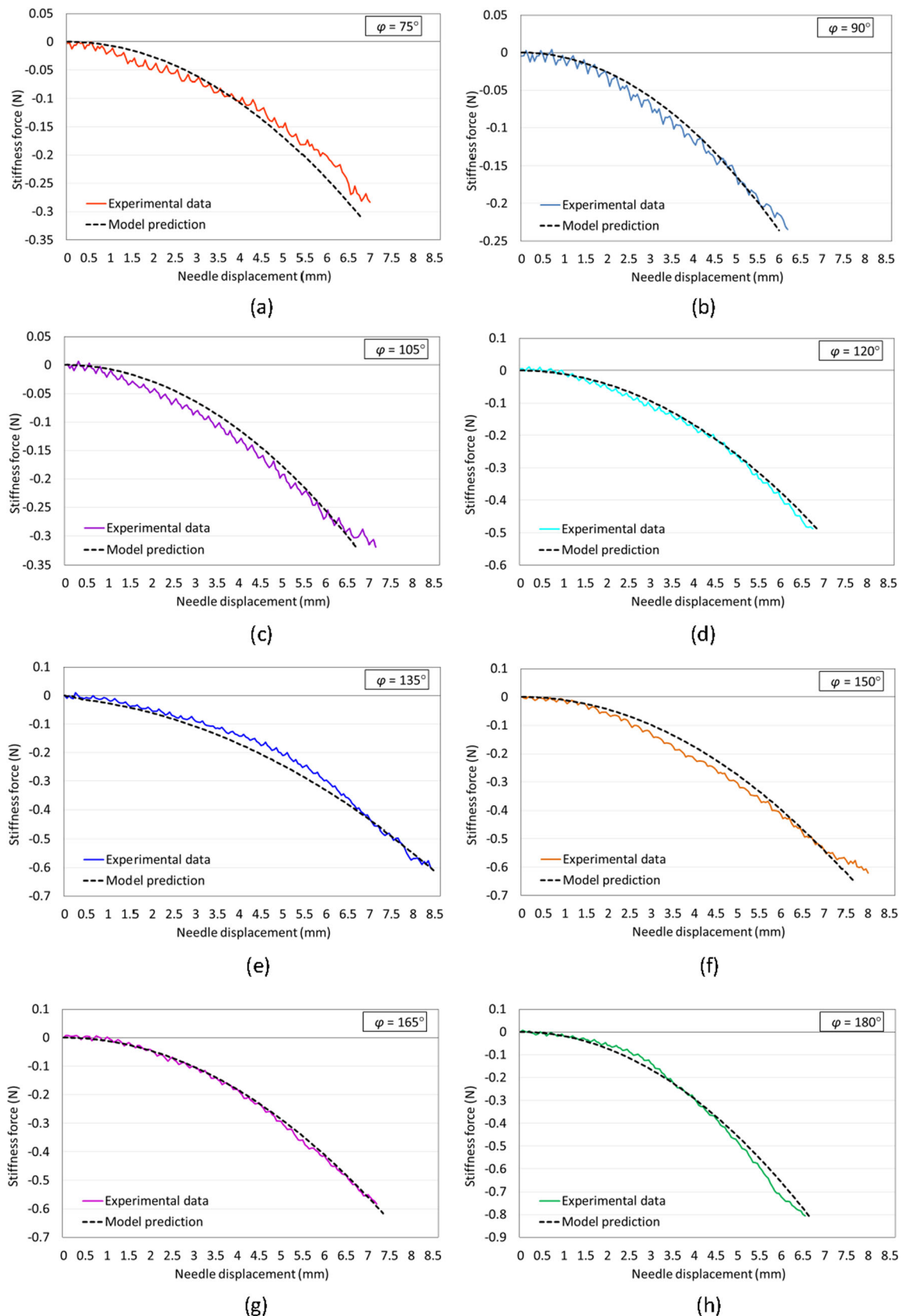
by Eq. (14) and Eq. (12). In addition, by using the least squares method to fit these data for  $C$ , we identified the statistical expression of  $C(\phi)$  as Eq. (28).

$$C(\phi) = \frac{1}{0.0541\phi^3 - 0.1246\phi^2 + 0.102\phi - 0.0498} - 4.7736 \quad (28)$$

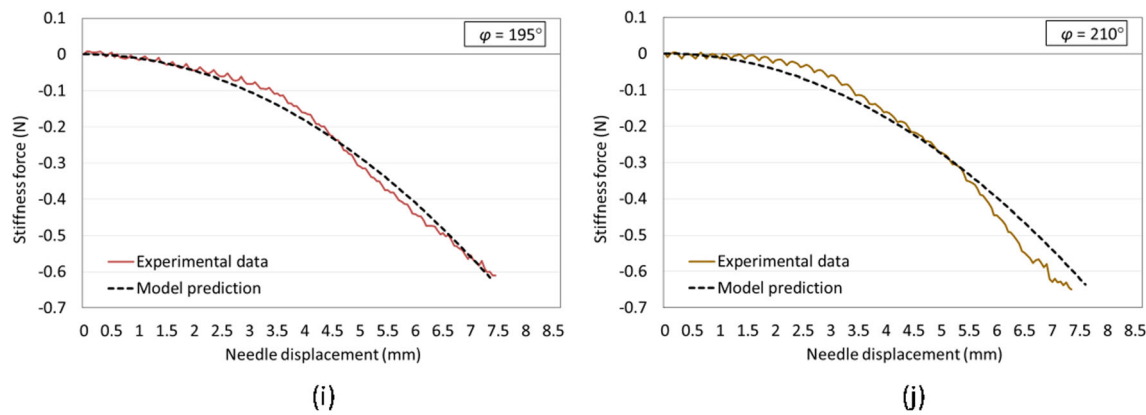
By combining Eq. (28) and Eq. (9), the increasing trend of the stiffness force could be predicted. By substituting Eq. (27) into Eq. (14), the maximum value of the stiffness force could be calculated. By combining Eq. (9) and Eq. (14), we could predict the stiffness force for different IOAs. Figure 6 shows the contrasting results between the model prediction and the tenth trial of the experimental data for each group of the test.

Considering the calculation model given by Eq. (15), by substituting Eq. (27) within it, we could compare the model-predicted value and the statistical expression in Eq. (28) of  $C(\phi)$  (Fig. 7).

Then, a similar processing method for the axial cutting force data, which we adopted in the pretest, was employed in the experiments. The axial cutting force of each test is displayed in Table 3.



**Fig. 6** Experimental and model prediction of stiffness force. **a**  $\varphi = 75^\circ$ , **b**  $\varphi = 90^\circ$ , **c**  $\varphi = 105^\circ$ , **d**  $\varphi = 120^\circ$ , **e**  $\varphi = 135^\circ$ , **f**  $\varphi = 150^\circ$ , **g**  $\varphi = 165^\circ$ , **h**  $\varphi = 180^\circ$ , **i**  $\varphi = 195^\circ$ , and **j**  $\varphi = 210^\circ$

**Fig. 6** (continued)

The test groups of  $\varphi \in [90^\circ, 180^\circ]$  contained the whole range of values of  $\phi$  and did not have the same value. Therefore, we took the average cutting force of each group in the range  $\varphi \in [90^\circ, 180^\circ]$  to calculate the five elastic parameters of the tissue mentioned in Eq. (20).

First, we transformed the axial cutting force into the force acting on the inclined plane of cutting by using:

$$F_c = F_{\text{caxis}} / \sin\alpha \quad (29)$$

where  $F_{\text{caxis}}$  is the axial cutting force that we obtained from the experiments. According to the model of the cutting force given in Eq. (18), we have:

$$E' = 4F_{\text{caxis}} \tan \frac{\alpha}{2} / (d^2 \sin\alpha) \quad (30)$$

Then, we placed the average value of the axial cutting force into Eq. (30) to calculate the corresponding values of the off-axis reduction stiffness coefficient. By combining Eq. (25a), we now had seven equations to obtain five elasticity parameters. By solving the overdetermined equations, we obtained the five independent elastic constants of the tissue (Table 4).

By substituting these parameters into Eq. (25b), and by combining Eq. (18) and Eq. (29), we could calculate the axial cutting force, which was dependent on  $\phi$ . The experimental

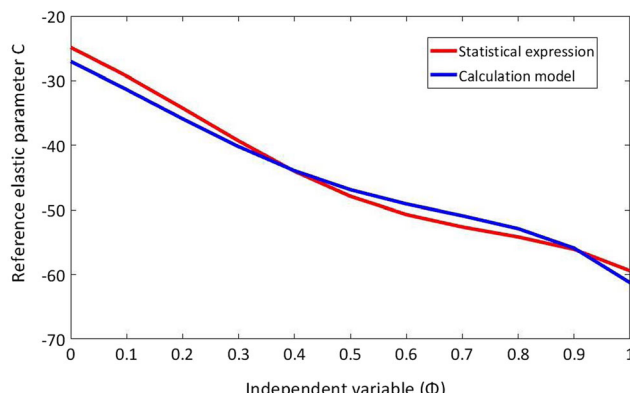
data and the model calculation curves of the axial cutting force are shown in Fig. 8.

Figure 6 shows that the force model could describe variations in the stiffness force and predict rupture events during the external contact stage with different orientation angles of the needle. Figure 7 shows the curve of the calculation model, and Eq. (15) coincided with the statistical expression of the reference elastic parameter. Figure 8 shows that the model curve could predict the axial cutting force of different IOAs.

## 4 Discussion

Comparing the data from the experiments and the model prediction, Table 5 displays the model's predicted error for different IOAs. The maximum predicted error of the maximum stiffness force is 0.033 N. During the external contact stage, the predicted error of the maximum needle displacement is less than 0.45 mm. Meanwhile, the maximum error of the predicted stiffness force is -0.089 N. The root-mean-squared-error (RMSE) of the predicted stiffness force for different IOAs is close to zero. The maximum predicted error of axial cutting force is -0.044 N. From Table 5, it is clear that the developed models successfully estimate the stiffness force and cutting force during needle insertion into the muscle tissue.

As described in Eq. (14), the variation in stiffness force was related to the IOA, shape of the needle tip, and tissue mechanics. Furthermore, based on Eq. (9), the maximum stiffness force was also dependent on these factors. When a needle with different IOAs was inserted into the soft tissue, the variation in the stiffness force could be visualized. As shown in Fig. 7, the stiffness force increased the slowest and had the lowest maximal absolute value when  $\phi = 1$ . However, the opposite situation appeared at  $\phi = 0$ . This phenomenon has been described previously [18, 21, 28–30]. The difference in the experimental maximum stiffness force between the test group  $\phi = 1$  and the test group  $\phi = 0$  is 0.572 N. The possible reason is related to

**Fig. 7** Calculation model and statistical expression of  $C(\phi)$

**Table 3** Axial cutting force of each group of test

Axial cutting force (N)										
$\varphi (\phi)$	75° (0.966)	90° (1)	105° (0.966)	120° (0.866)	135° (0.707)	150° (0.5)	165° (0.259)	180° (0)	195° (0.259)	210° (0.5)
1	-0.2052	-0.1897	-0.2011	-0.2243	-0.2875	-0.3326	-0.3792	-0.4599	-0.3820	-0.3326
2	-0.1978	-0.1924	-0.2102	-0.2235	-0.2866	-0.3323	-0.3805	-0.4653	-0.3833	-0.3315
3	-0.2076	-0.1905	-0.2029	-0.2196	-0.2898	-0.3328	-0.3816	-0.4661	-0.3794	-0.3337
4	-0.2023	-0.1953	-0.2016	-0.2188	-0.2793	-0.3319	-0.3868	-0.4579	-0.3801	-0.3357
5	-0.1989	-0.1922	-0.2074	-0.2217	-0.2806	-0.3288	-0.3807	-0.4688	-0.3788	-0.3336
6	-0.1909	-0.1918	-0.2033	-0.2229	-0.2870	-0.3405	-0.3832	-0.4590	-0.3796	-0.3329
7	-0.2007	-0.1927	-0.2058	-0.2202	-0.2858	-0.3325	-0.3795	-0.4643	-0.3822	-0.3342
8	-0.2019	-0.1914	-0.2047	-0.2301	-0.2903	-0.3330	-0.3799	-0.4637	-0.3817	-0.3350
9	-0.2020	-0.1925	-0.2035	-0.2256	-0.2828	-0.3297	-0.3838	-0.4641	-0.3813	-0.3352
10	-0.2029	-0.1917	-0.2056	-0.2208	-0.2878	-0.3311	-0.3830	-0.4632	-0.3825	-0.3344
Average	-0.2010	-0.1920	-0.2046	-0.2228	-0.2873	-0.3325	-0.3818	-0.4635	-0.3811	-0.3339

the direction of the fracture of the tissue material. If  $\phi = 1$ , the tissue is separated at a direction that is perpendicular to the fibers; so, fracture events are contributed mainly by the fiber matrix. Along with the decrease in  $\phi$ , more fibers will be included in the fracture direction until reaching the maximum value at  $\phi = 0$ . The stiffness force model that was developed in this paper has been quantized to clarify this phenomenon.

The cutting force acting on the needle tip has axial and transverse components. The axial component was measured in the experiments, and we calculated the cutting force by Eq. (29). According to Eq. (16) and Eq. (25a) and Eq. (25b), the cutting force is related to the geometric characteristics and IOA of the needle. The cutting force will be a constant if the IOA is a fixed value (no rotation during needle insertion, and needle bending is negligible). The calculation results of this quantitative analytic model of the cutting force are in accordance with those of the qualitative studies [11, 20]. Our experiments showed that the axial cutting force was clearly dependent on variations in the IOA. The cutting force reached a maximal absolute value when  $\phi = 0$  and was lowest when  $\phi = 1$ . The maximal difference of the cutting force was 0.271 N. Table 4 shows that  $|\hat{C}_{11}| \ll |\hat{C}_{33}|$ ;  $\hat{C}_{11}$  represents the stiffness of the fiber matrix and  $\hat{C}_{33}$  represents the fiber stiffness. This is further evidence that the direction of the rupture event has an effect on the insertion force because of the cutting angle to the fibers. As  $\phi$  gets closer to zero, the needle suffers a larger cutting force and, then, bends more at the next insertion step. Needle deflection would change the orientation of the needle tip in the tissue space and result in a variation of the cutting

force. That is, the needle would experience dynamic curvature changes during the inside cutting stage. The quantitative analytic model that was developed in this paper could modify the hypothesis of constant cutting force in a previous study [1, 11, 12, 20].

From the experimental results, it can be seen that the elasticity of the fiber-structured tissue is not isotropic, and it clearly has an important impact on the insertion force. The developed model matched the experimental data of the stiffness force and the cutting force, and it showed the variations in these forces upon needle insertion into the transverse isotropic soft tissue. The force difference for different IOAs can also be clearly described. Because the presented method accounts for the influence of the needle tip orientation, it will be more applicable for transverse isotropic soft tissue compared to the isotropic insertion force model.

Tissue–needle coupling interaction deformation is another important issue during needle insertion. The transverse component of the cutting force will cause nonlinear needle deflection [12]. The tissue around the curving needle axis is compressed and occurs in nonlinear deformation. However, this

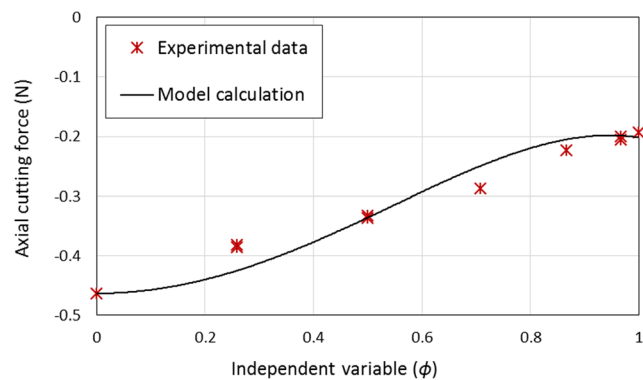


**Fig. 8** Experimental data and model-predicted curve of the axial cutting force

**Table 4** Independent elastic constants of the tissue

$\hat{C}_{11}$	$\hat{C}_{33}$	$\hat{C}_{12}$	$\hat{C}_{13}$	$\hat{C}_{44}$
$0.19 \times 10^{-5}$	-2.018	-0.033	-1.042	1.530

**Table 5** Model-predicted error for different IOAs

$\varphi$	75°	90°	105°	120°	135°	150°	165°	180°	195°	210°
Predicted error of maximum stiffness force (N)										
Error	0.028	0.002	0.001	0.001	0.015	0.025	0.033	0.003	0.005	-0.013
Predicted error of maximum needle displacement (mm)										
Error	0.2	0.25	0.45	-0.1	-0.1	0.35	-0.15	-0.1	0.1	-0.25
Predicted error of stiffness force (N)										
Maximum error	0.050	0.021	-0.027	-0.028	0.053	-0.053	-0.025	-0.071	-0.037	-0.089
RMSE	0.020	0.009	0.015	0.012	0.024	0.026	0.009	0.026	0.018	0.035
Predicted error of axial cutting force (N)										
Error	0.001	-0.009	0.007	0.017	0.037	0.001	-0.039	0.002	-0.044	-0.003

issue is beyond the scope of this paper. As mentioned previously, we used a depth of needle insertion that was less than 40 mm to minimize the effect of the interaction deformation as much as possible. Neglecting the effect of this nonlinear deformation in the limited insertion depth made the force models succinct. However, when the needle axis deflects or rotates in the tissue, a real-time update in the off-axis reduction stiffness coefficient according to the needle tip's pose will enhance the accuracy of force prediction.

## 5 Conclusion

Mechanics-based models are developed to predict the stiffness force and the cutting force acting on the needle tip during needle insertion in transverse isotropic soft tissue. The proposed approach analyzed three events, including needle-tissue contact, tissue surface rupture, and tissue cutting. The contact model shows the variation in stiffness force for different IOAs, and the modified fracture-based model was able to calculate the corresponding maximum value of the puncturing force. By combining the two models, we could predict the stiffness force when the needle tip contacts the transverse isotropic tissue for the arbitrary insertion orientation angle. Using the novel cutting force model proposed in this paper, we could show the relationship between the needle tip pose and the cutting force during needle inserts in transverse isotropic tissue. A series of needle insertion experiments were performed on ex vivo porcine tissue sample to obtain the model parameters and to validate the analytical predictions. The proposed approach accurately predicts the stiffness force and the cutting force during needle insertion in the transverse isotropic tissue.

In future works, we will separately analyze the tissue nonlinear deformation force and relate needle nonlinear deflection to the cutting force model in the 3D transverse isotropic space. Moreover, we plan to investigate needle steering in robot-assisted automatic percutaneous puncture based on the developed force model and needle deflection model.

**Acknowledgments** The authors would like to thank Mr. H Suo for his contribution to the experiment design and data collection. The authors would also like to thank Dr. C Suo and Dr. BB Farouk for their help in proofreading the manuscript.

This work was supported by the National Natural Science Foundation of China (No. 51775368 and No. 51811530310).

**Publisher's note** Springer Nature remains neutral with regard to jurisdictional claims in published maps and institutional affiliations.

## References

1. Abayazid M (2015) Robotically steering flexible needles. Ph.D. dissertation, Dept. Faculty of Eng Tech, Twente Univ, Enschede, Netherlands
2. Adebar TK, Greer JD, Laeseke PF, Hwang GL, Okamura AM (2016) Methods for improving the curvature of steerable needles in biological tissue. *IEEE Trans Biomed Eng* 63:1167–1177
3. Barnett AC, Lee YS, Moore JZ (2016) Fracture mechanics model of needle cutting tissue. *ASME J Manuf Sci Eng* 138:011005
4. Bischoff JE, Arruda EM, Grosh K (2004) A rheological network model for the continuum anisotropic and viscoelastic behaviour of soft tissue. *Biomech Model Mechanobiol* 3:56–65
5. Böhl M, Kruse R, Ehret AE, Leichsenring K, Siebert T (2012) Compressive properties of passive skeletal muscle—the impact of precise sample geometry on parameter identification in inverse finite element analysis. *J Biomech* 45:2673–2679
6. Böhl M, Ehret AE, Leichsenring K, Weichert C, Kruse R (2014) On the anisotropy of skeletal muscle tissue under compression. *Acta Biomater* 10:3225–3234
7. Carra A, Avilavilchis JC (2010) Needle insertion modeling through several tissue layers. 2010 2nd International Asia Conference on CAR, pp 237–240
8. Cowin SC (2013) Continuum mechanics of anisotropic materials. Springer, New York, pp 83–99
9. Feng Y, Lee CH, Sun L, Okamoto RJ, Ji S (2015) Automated estimation of elastic material parameters of a transversely isotropic material using asymmetric indentation and inverse finite element analysis. *ASME 2015 International Mechanical Engineering Congress and Exposition*, pp V003T03A007
10. Hing JT, Brooks AD, Desai JP (2006) Reality-based needle insertion simulation for haptic feedback in prostate brachytherapy. *IEEE International Conference on Robotics Automation*, pp 619–624
11. Jiang S, Li P, Yu Y, Liu J, Yang ZY (2014) Experimental study of needle-tissue interaction forces: effect of needle geometries, insertion methods and tissue characteristics. *J Biomech* 47:3344–3353

12. Khadem M, Fallahi B, Rossa C, Sloboda RS (2015) A mechanics-based model for simulation and control of flexible needle insertion in soft tissue. IEEE International Conference on Robotics Automation, pp 2264–2269
13. Khadem M, Rossa C, Sloboda RS, Usmani N, Tavakoli M (2017) Mechanics of tissue cutting during needle insertion in biological tissue. IEEE Robot Autom Lett 1:800–807
14. Lendvay TS, Hsieh FJ, Hannaford B, Rosen J (2008) The biomechanics of percutaneous needle insertion. 16th Conference on Medicine Meets Virtual Reality, pp 245–247
15. Li P, Jiang S, Liang D, Yang ZY, Yu Y, Wang W (2017) Modeling of path planning and needle steering with path tracking in anatomical soft tissues for minimally invasive surgery. Med Eng Phys 41: 35–45
16. Mahvash M, Hayward V (2001) Haptic rendering of cutting, a fracture mechanics approach. Haptics-e 2:1–12
17. Mahvash M, Dupont PE (2010) Mechanics of dynamic needle insertion into a biological material. IEEE Trans Biomed Eng 57:934–943
18. Ní Annaidh A, Bruyère K, Destrade M, Gilchrist MD, Otténio M (2012) Characterization of the anisotropic mechanical properties of excised human skin. J Mech Behav Biomed Mater 28:139–148
19. Ní Annaidh A, Bruyère K, Destrade M, Gilchrist MD, Maurini C, Otténio M (2012) Automated estimation of collagen fiber dispersion in the dermis and its contribution to the anisotropic behavior of skin. Ann Biomed Eng 40:1666–1678
20. Okamura AM, Simone C, O'Leary MD (2004) Force modeling for needle insertion into soft tissue. IEEE Trans Biomed Eng 51:1707–1716
21. Ottenio M, Tran D, Ní AA, Gilchrist MD, Bruyère K (2015) Strain rate and anisotropy effects on the tensile failure characteristics of human skin. J Mech Behav Biomed Mater 41:241–250
22. Ridge MD, Wright V (1966) Mechanical properties of skin: a bioengineering study of skin structure. J Appl Physiol 21:1602–1606
23. Rossa C, Lehmann T, Sloboda R, Usmani N, Tavakoli MC (2017) A data-driven soft sensor for needle deflection in heterogeneous tissue using just-in-time modelling. Med Biol Eng Comput 55: 1401–1414
24. Ruvolo EC Jr, Stamatias GN, Kollias N (2007) Skin viscoelasticity displays site- and age-dependent angular anisotropy. Skin Pharmacol Physiol 20:313–321
25. Tai Y, Wei L, Zhou H, Nahavandi S, Shi J (2016) Tissue and force modelling on multi-layered needle puncture for percutaneous surgery training. IEEE International Conf on SMC, pp 002923–002927
26. Takaza M, Moerman KM, Gindre J, Lyons G, Simms CK (2013) The anisotropic mechanical behaviour of passive skeletal muscle tissue subjected to large tensile strain. J Mech Behav Biomed Mater 17:209–220
27. Tanaka N, Higashimori M, Kaneko M, Kao I (2011) Noncontact active sensing for viscoelastic parameters of tissue with coupling effect. IEEE Trans Biomed Eng 58:509–520
28. Van LM, Lyons CG, Simms CK (2006) A validated model of passive muscle in compression. J Biomech 39:2999–3009
29. Van LM, Simms CK, Lyons CG (2009) Viscoelastic properties of passive skeletal muscle in compression-cyclic behavior. J Biomech 42:1038–1048
30. Wong WLE, Joyce TJ, Goh KL (2016) Resolving the viscoelasticity and anisotropy dependence of the mechanical properties of skin from a porcine model. Biomech Model Mechanobiol 15:433–446



**Wanyu Liu** is a PhD student in the School of Mechanical Engineering at Tianjin University. Her research interest includes 6-DOF force sensor technology, force modeling, and force feedback control system of medical robots.



**Zhiyong Yang** is a Professor in the School of Mechanical Engineering at Tianjin University. He is interested on nonlinear dynamics, automatics, minimally invasive surgical robots, and motion control.



**Pan Li** is a PhD student in the School of Mechanical Engineering at Tianjin University. Her research interest includes force modeling, virtual simulation, motion planning, and control of medical robots.



**Jianpeng Zhang** is a postgraduate student in the School of Mechanical Engineering at Tianjin University. His research interest includes deformation simulation and control algorithm of flexible needle.



**Shan Jiang** is a Professor in the School of Mechanical Engineering at Tianjin University. She is interested on medical image processing, surgical treatment planning, and medical robot-assisted surgery.